Computers & Geosciences 185 (2024) 105546

Contents lists available at ScienceDirect

Computers and Geosciences

journal homepage: www.elsevier.com/locate/cageo

Research Paper

A fast and robust method for detecting trend turning points in InSAR displacement time series

Ebrahim Ghaderpour *, Benedetta Antonielli, Francesca Bozzano, Gabriele ScarasciaMugnozza, Paolo Mazzanti

Department of Earth Sciences & CERI Research Centre, Sapienza University of Rome, P.le Aldo Moro, 5, Rome 00185, Italy
NHAZCA s.r.l., Via Vittorio Bachelet, 12, Rome 00185, Italy

ARTICLE INFO

Keywords:
Change detection
Ground deformation
Ordinary least-squares
Pettitt's test
PS-InSAR time series
Trend turning point

ABSTRACT

Ground deformation monitoring is a crucial task in geohazard management to ensure the safety of lives and infrastructure. Persistent scatterer interferometric synthetic aperture radar (PS-InSAR) is an advanced technique for measuring small displacements on the Earth's surface. Estimated PS-InSAR time series acquired by Sentinel-1 satellites provide a great opportunity for effective monitoring of ground deformation in recent years. However, challenges arise when processing these time series due to their non-uniform sampling, noise from atmosphere and preprocessing issues including phase unwrapping and others. Therefore, estimating the location and direction of trend turning in such time series, as an indicator of ground deformation, is not an easy task. In this work, a sequential turning point detection method (STPD) is proposed and compared with other change point detection methods. Using a large set of simulated time series with various noise types, it is shown that STPD outperforms other methods in terms of overall accuracy and root mean square error for location and direction of trend turnings. As a case study, STPD is applied to detect turning points within PS-InSAR time series for the province of Frosinone in Italy and classified using topography and land cover/use. In addition, an area susceptible to landslides is selected to estimate the starting dates of potential slow-moving landslides. It is also shown that the turning points in the local precipitation time series have a high correlation with the ones in the PS-InSAR time series, indicating that precipitation is a major triggering factor of the displacements in the area. The STPD can rapidly and effectively detect locations and directions of trend turnings and is freely available online in both MATLAB and python.

1. Introduction

Ground deformation is a phenomenon that may have anthropogenic or natural origin and can cause severe environmental and socioeconomic impacts (Cascini et al., 2009; Cianflone et al., 2015; Coda et al., 2019). Various factors can cause ground to deform slowly or rapidly, such as groundwater exploitation and abstraction, volcanic activities, earthquake-triggered landslides, rockfalls, and many others (Varnes, 1978; De Martino et al., 2021; Martino et al., 2022; Kundu et al., 2023). Deformation in mountainous regions is usually as a result of landslides, mudslides, rockfalls, etc., and its susceptibility analysis is based on topography (Nakileza and Nedala, 2020; Martino et al., 2022; Kundu et al., 2023). In urbanized regions, groundwater fluctuations (subsidence or uplift) may occur due to anthropogenic activities, e.g., land subsidence as a result of extensive groundwater extraction for industry or agriculture (Bai et al., 2016; Coda et al., 2019; Allocca et al., 2022). Other types man-made ground deformation include urbanization, building and road reconstruction.

Persistent scatterer interferometric synthetic aperture radar (PS-InSAR) has been utilized in various studies for ground deformation monitoring, such as land subsidence and uplift in urban areas, landslides, and small-scale tectonic activity (Mateos et al., 2017; Hussain et al., 2022; Yao et al., 2022; Makabayi et al., 2021; Wang et al., 2022). Sentinel 1 A and 1B satellites travel half of their trajectory from the south pole to the north pole (ascending orbit) and the other half from north pole to south pole (descending orbit), Fig. 1. The satellites revisit the same area along both orbits, and so both ascending and descending data are acquired over the same area in different times, allowing to estimate the vertical and east–west components of displacement (Ren et al., 2022). There are several challenges when processing PS-InSAR time series. For example, phase unwrapping is a crucial task in InSAR techniques to resolve the ambiguity of modulo 2π and obtain the

* Corresponding author at: Department of Earth Sciences & CERI Research Centre, Sapienza University of Rome, P.le Aldo Moro, 5, Rome 00185, Italy.
E-mail address: ebrahim.ghaderpour@uniroma1.it (E. Ghaderpour).

https://doi.org/10.1016/j.cageo.2024.105546
Received 17 August 2023; Received in revised form 4 December 2023; Accepted 23 January 2024
Available online 29 January 2024

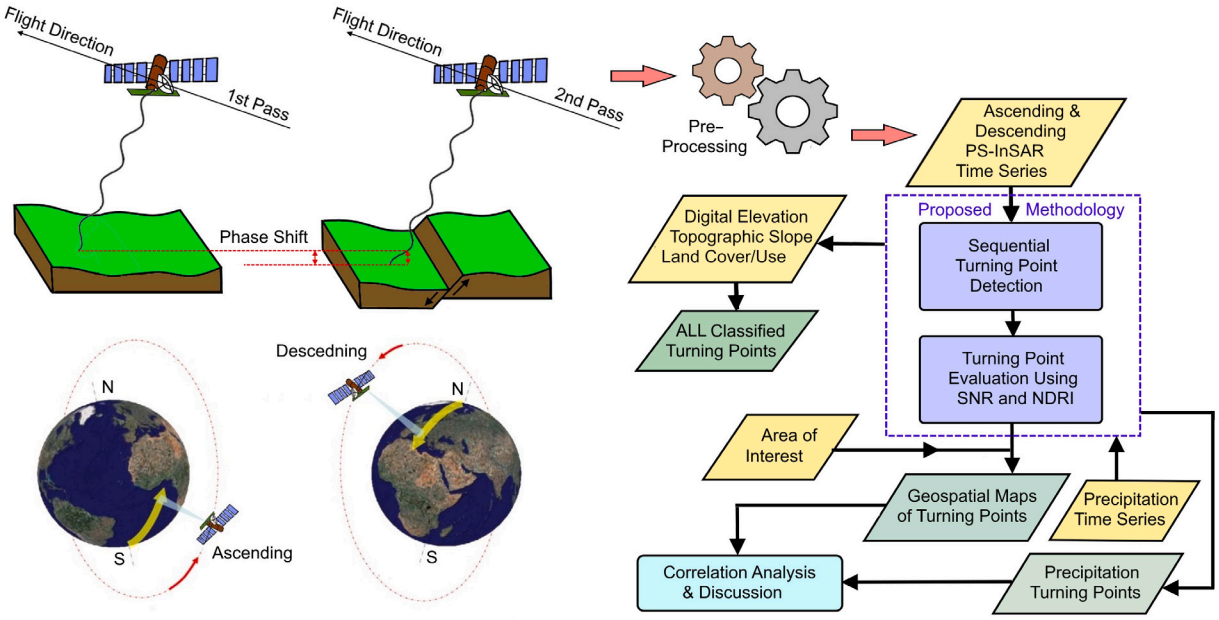

Fig. 1. The flowchart of this work.

absolute change of phase for before estimating displacement; however, this pre-processing can lead to undesired biases in the displacement time series (Zeyada et al., 2022). The deformation curves in PS-InSAR time series are usually discrete with error though their cumulative deformation and velocity are usually very good (Zhang et al., 2011; Yao et al., 2022). The PS-InSAR generally coincides with buildings, artificial structures, and non-vegetated areas (Makabayi et al., 2021). As the direction of the ground deformation approaches to the direction of the flightpath, i.e., north-south direction, the SAR echoes become less sensitive, failing to properly measure the displacement toward that direction (Moretto et al., 2021).

A turning point (TP) is a location in a time series where the gradient changes while a change point (CP) in the time series can be a jump (datum shift) or a TP or others. Herein, a CP is distinguished from a TP, i.e., a TP is always a CP but a CP may not be necessarily a TP (e.g., datum shift). In geology, changes in displacement time series may be abrupt (e.g., due to earthquakes, rockfalls, etc.) or because of slow-moving ground deformation or landslides causing a turn in displacement trend (Cianflone et al., 2021; Hussain et al., 2021; Lattari et al., 2022). Popular CP detection methods applied in climatology, geology, and environmental sciences include but are not limited to non-parametric, Bayesian-based, and machine learning methods (Jaiswal et al., 2015; Aminikhanghahi and Cook, 2017; Ghaderpour et al., 2021; Lattari et al., 2022). However, most of CP detection methods in literature have a high computational cost for applications, such as processing millions of PS-InSAR time series (Awty-Carroll et al., 2019). Furthermore, it can be very challenging to identify whether a detected change by a model is a true TP, jump, or phenological change, because these types of changes may easily be confused in the model when the noise level is high or the time series are not regularly sampled (Awty-Carroll et al., 2019; Ghaderpour et al., 2021). Therefore, developing a fast and reliable TP detection method becomes crucial. The flowchart of this work is shown in Fig. 1, and the main contributions of this study are summarized below.

(1) Developing a robust TP detection method to rapidly detect and categorize TPs.

(2) Comparing three CP detection methods with the proposed method.

(3) Applying the proposed method to detect TPs in PS-InSAR time series for the province of Frosinone in Italy.

(4) Classifying the detected TPs using topography and land cover/use for Frosinone.

(5) Investigating the correlation between precipitation and displacement TPs within an area susceptible to landslides.

2. Methods

In Section 2.1, three existing CP detection methods are reviewed, namely, Pettitt's test, running slope difference (RSD), and sequential change point detection (SCPD). Then in Section 2.2, a robust TP detection method is proposed, namely, sequential turning point detection (STPD).

2.1. Existing change detection methods

2.1.1. Pettitt's test

Pettitt's test is a popular non-parametric statistical test for detecting CPs in time series (Pettitt, 1979; Li and Pi, 2022; Gourgouletis and Baltas, 2023). Let $\{y_1, \ldots, y_n\}$ be a series of n random variables or observations. Let F_1 and F_2 be the distribution functions of segments $\{y_1, \ldots, y_\tau\}$ and $\{y_{\tau+1}, \ldots, y_n\}$, respectively, where τ is a potential CP. The null (H_0) and alternative (H_1) hypotheses are defined as

$$\begin{cases} H_0: & F_1 = F_2 \quad \text{(no CP)} \\ H_1: & F_1 \neq F_2 \quad \text{(CP at time } \tau\text{)} \end{cases} \tag{1}$$

To detect the CP for each t ($1 \leq t < n$), the following test statistics is calculated that is like Mann–Whitney test statistic (Mann and Whitney, 1947):

$$U_{t,n} = \sum_{i=1}^{t} \sum_{j=t+1}^{n} \operatorname{sgn}(y_i - y_j), \qquad 1 \leq t < n \tag{2}$$

where

$$\operatorname{sgn}(x) = \begin{cases} 1 & \text{if } x > 0 \\ 0 & \text{if } x = 0 \\ -1 & \text{if } x < 0 \end{cases} \tag{3}$$

The most probable CPs are obtained by

$$K_\tau = \max_{1 \leq t < n}(|U_{t,n}|), \tag{4}$$

If there are multiple τ ($1 \leq \tau < n$) satisfying Eq. (4), then the one that has the minimum distance to $n/2$ is considered the most probable CP. The p-value of Pettitt's test is approximated by

$$p \approx 2\exp\left(\frac{-6K_\tau^2}{n^2+n^3}\right). \tag{5}$$

Given a significant level α (usually 0.05 or 0.01), if $p < \alpha$, then the null hypothesis is rejected which means the distributions of the two segments are different, i.e., there is CP at τ. Once the CP is determined, the gradient of each segment can be estimated by Sen's slope estimator (Shawky et al., 2023; Zaghloul et al., 2022).

2.1.2. Running slope difference

The running slope difference (RSD), proposed by Zuo et al. (2019), is a CP detection method applied to climate time series. The RSD is based on a sequential fitting of linear trend with two pieces to segments of a time series. Mathematically, suppose that $S_1 = \{y_1, \ldots, y_\tau\}$ and $S_2 = \{y_{\tau+1}, \ldots, y_n\}$ are two segments of a time series of size n, where τ is the potential TP ($1 < \tau < n$). The RSD models these segments by

$$y_i = m_1 x_i + b_1 + \varepsilon_i, \quad \text{for } 1 \leq i \leq \tau, \tag{6}$$

$$y_j = m_2 x_j + b_2 + \varepsilon_j, \quad \text{for } \tau < j \leq n. \tag{7}$$

where m_1 and m_2 are the gradients, b_1 and b_2 are the intercepts, and ε_i and ε_j are the error terms to be estimated by the ordinary least-squares method (OLS) (Zuo et al., 2019; Ghaderpour and Vujadinovic, 2020). The test statistics for the gradient is defined as

$$t_{\text{gradient}} = \frac{\widehat{m}_1 - \widehat{m}_2}{S_{\widehat{m}_1,\widehat{m}_2}} \tag{8}$$

where the hat symbol means estimation and $S^2_{\widehat{m}_1,\widehat{m}_2}$ is the estimated variance of $\widehat{m}_1 - \widehat{m}_2$ that is equal to $S^2_{\widehat{m}_1} + S^2_{\widehat{m}_2}$ when the observations are statistically independent. It can be verified that Eq. (8) follows the t-distribution with $n-4$ degrees of freedom if the error terms ε_i and ε_j are normally distributed independent random variables with zero mean and variance σ^2, where 4 degrees are lost due to the estimations of two gradients and two intercepts (Zuo et al., 2019). The null (H_0) and alternative (H_1) hypotheses in RSD are defined as

$$\begin{cases} H_0: & m_1 = m_2 \quad \text{(no CP)} \\ H_1: & m_1 \neq m_2 \quad \text{(CP at time } \tau\text{)} \end{cases} \tag{9}$$

If $|t_{\text{gradient}}| > t_{n-4,1-\alpha/2}$ at a given significance level α, then the null hypothesis is rejected, and there is a gradient CP occurring at τ at $100(1-\alpha)\%$ confidence level (Zuo et al., 2019).

For each τ, $1 < \tau < n$, OLS will estimate a gradient and an intercept for Eq. (6) (first piece) and another independent gradient and independent intercept for Eq. (7) (second piece). The criterion for selecting a CP in RSD is maximizing the absolute gradient difference value (Zuo et al., 2019). As demonstrated in the results section, this criterion more frequently can lead to false detection of TP location as compared to minimizing L2 norm of residuals.

The running approach in RSD is based on a translating window where the two trend pieces, Eqs. (6) and (7), have the same size, i.e., the window center is the place where the gradients of the two pieces are estimated to obtain a gradient difference. Then the window translates and a gradient difference will be estimated for each window to create a RSD time series (Zuo et al., 2019). The local maximum and minimum values of the RSD time series are the potential CPs if they are statistically significant.

There are some shortcomings for this approach. First, for a large window size, no CPs can be detected for the first or second half of the window. For example, for a 4-year-long window, RSD cannot detect any change in 2015, 2016, 2020, and 2021 for the 7-year-long PS-InSAR time series employed in this work. On the other hand, reducing the size of the window can easily increase the false positive rate due to existence of inter-annual and seasonal noise or serial correlation. Second, local exterma of the RSD time series cannot always provide the true location of CPs when dealing with various noise types. One way to overcome these limitations is using a large window size (e.g., 5-year-long) but sequentially estimate the gradient differences within the window and choose the time index corresponding to the maximum of their absolute values as a potential CP. Herein, this method is referred to modified RSD (MRSD).

2.1.3. Sequential change point detection

The SCPD sequentially fits a linear trend with two pieces within a window, where an independent intercept and an independent slope are estimated for each linear piece sequentially and within the window, like MRSD. However, the criterion for detecting a CP in SCPD is minimizing the residual norm not maximizing the absolute value of the gradient difference. In fact, SCPD is a special case of jumps upon spectrum and trend (JUST) which only uses trend fitting without any simultaneous harmonic fitting (Ghaderpour and Vujadinovic, 2020; Ghaderpour, 2021). Using simulated time series, it is shown herein that minimizing the residual norm performs better than maximizing the absolute value of the gradient difference for TP detection.

2.2. Proposed methodology

The RSD is sensitive to jumps (datum shift) starting at τ, i.e., the estimated pieces can be discontinuous at τ, see Eqs. (6) and (7). In practice, jumps of low magnitudes may have been caused during the preprocessing and phase unwrapping of InSAR time series while higher magnitude jumps could be due to earthquakes, rockfalls, volcanic activities, and others causing a sudden and large datum shift in the time series values which are not the focus of this work. Since the goal of this study is detecting TP in InSAR time series that often exhibit jumps of low magnitudes, it is assumed that the linear trend may show a TP without jump, i.e., the fitted linear trend is continuous and has a TP where the gradient changes (no datum shift). The proposed TP detection method uses a windowing technique where a sequential approach is performed within each window to estimate a potential TP. For simplicity, Section 2.2.1 describes the sequential approach within one window. Then the windowing strategy in STPD is described in Section 2.2.2.

2.2.1. Sequential turning point detection

For a given window, STPD has two steps: forward and backward estimations.

Step 1. In the forward estimation, like RDS, m_1 and b_1 in Eq. (6) are estimated by OLS, but only m_2 in Eq. (7) is estimated while b_2 is replaced by $\widehat{b}_2 = \widehat{m}_1 x_\tau + \widehat{b}_1$ with $x_j \leftarrow x_j - x_\tau$, $\tau \leq j \leq n$. The residual series, the estimated linear trend with TP at τ subtracted from the entire time series, is calculated for each τ, $1 < \tau < n$. The potential TP τ_{forward}, $1 < \tau_{\text{forward}} < n$, is the one minimizing the L2 norm of the residual series.

Step 2. In the backward estimation, the time series is flipped and the forward estimation process in Step 1 is applied to estimate the linear trend with a potential TP. Then this linear trend is flipped to get the TP τ_{backward}, $1 < \tau_{\text{backward}} < n$.

There is a potential TP in the time series if $|\tau_{\text{forward}} - \tau_{\text{backward}}|$ is close enough to zero. It is recommended a maximum difference of three points which corresponds to three months difference in the monthly resampled InSAR time series. Therefore, if $0 < |\tau_{\text{forward}} - \tau_{\text{backward}}| \leq 3$, then the potential TP will be the one that has the lowest L2 norm of residuals.

The test statistics of STPD is the same as RSD shown in Eq. (8), where $S_{\widehat{m}_2}$ is estimated from the model without the intercept component. The null and alternative hypotheses also remain the same as RSD with degrees of freedom one more than RSD as the second trend piece does not have the intercept component. The significance level selected

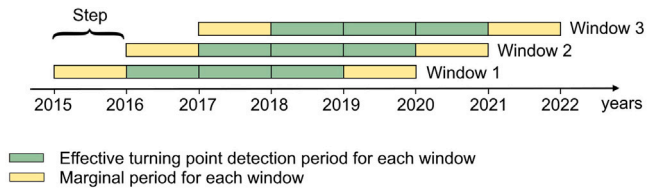

Fig. 2. The windowing strategy for the proposed TP detection method.

in this work is $\alpha = 0.01$, i.e., the selected τ must also be statistically significant at 99% confidence level.

Since STPD is designed for detecting TPs only (not jumps), it is crucial to define a measure to flag jumps; otherwise, the gradients of the linear pieces may not be a good indicator of gradual changes. To do so, a statistical metric, namely, normalized difference residual index (NDRI) is defined as follows:

$$\text{NDRI} = \frac{\|\vec{r}_1\| - \|\vec{r}_2\|}{\|\vec{r}_1\| + \|\vec{r}_2\|} \tag{10}$$

where $\|\cdot\|$ is the L2 norm, $\vec{r}_1$ and $\vec{r}_2$ are the residual series of the first and second time series segments with TP at τ, respectively, i.e., $\vec{r}_1$ is $\{y_i - \hat{m}_1 x_j - \hat{b}_1, \quad 1 \le i \le \tau\}$ and $\vec{r}_2$ is $\{y_j - \hat{m}_2 x_j - \hat{b}_2, \quad \tau \le j \le n\}$. When the absolute value of NDRI, corresponding to a detected TP, is close to one, it is likely that the TP is incorrectly detected due to a possible jump (datum shift) or poor data quality. A NDRI close to zero indicates a more reliable detected TP; however, choosing the threshold very close to zero reduces the sensitivity while increasing the specificity of the model. In Section 3, an optimal threshold for this metric is obtained. Another metric for evaluating the quality of TPs is signal-to-noise ratio (SNR), defined as the L2 norm of the trend divided by the L2 norm of the noise (white, seasonal, etc.).

2.2.2. *Windowing strategy in STPD*

To better understand the windowing strategy in STPD, an example is presented herein. Fig. 2 shows this strategy for a 7-year-long InSAR time series. Note that in the computer code, users may choose any window and step sizes to process their datasets. Herein, a fixed 5-year-long window for InSAR time series is chosen due to relatively poor SNR because of seasonality and slow-moving ground deformation. In this research, PS-InSAR time series are first re-sampled to a monthly scale using the spline interpolation technique. This will help mitigating over/under-estimation of linear trends due to the effect of missing values and extreme values (outliers). Note that for the sake of computational efficiency, STPD is only based on linear trend fitting not iterative season-trend fitting, and so equally spaced time series can be more effective and reliable.

Utilizing the monthly re-sampled time series, each window contains 60 samples, and so in the STPD forward and backward estimations described in Section 2.2.1, an optimal τ, $12 < \tau < 49$, is estimated by OLS, minimizing the residual L2 norm. Let τ_1, τ_2, and τ_3 be the potential detected TPs for windows 1, 2, and 3, respectively (Fig. 2) at 99% confidence level, i.e., a potential TP between 2016 and 2019, another one between 2017 and 2020, and another one between 2018 and 2021.

Next step is to evaluate the detected TPs. In this step, if the detected TPs from two consecutive windows are close enough to each other (i.e., within one year time difference), then the TP that is further away from the center of its corresponding window will be eliminated. For example, in Fig. 2, if TP τ_1 is in December 2018 in window 1 and TP τ_2 is in January 2018 in window 2, then τ_2 is more likely to be the true TP as it is closer to the center of window 2 (June 2018) while τ_1 is further away from the center of window 1 (June 2017). A detected trend closer to a window center is more likely to be a true TP as it has data supports from both side of the window, i.e., more robust to noise, such as inter-annual noise or strong serial correlation (Ghaderpour and Vujadinovic, 2020).

After determining k potential TPs (in this study $k \le 3$), a forward trend estimation process as described in Section 2.2.1 will be implemented to estimate an optimal linear trend with k TPs for the entire time series. A backward trend estimation process will also be implemented on the flipped time series with flipped TPs to estimate another optimal linear trend with the k TPs. From the forward and backward estimated trends, the trend whose residual norm is smaller will be chosen as the final optimal trend with k TPs. In other words, in the forward estimation, only the first linear trend piece has an unknown intercept to be estimated while in the backward estimation, only the last piece has an unknown intercept to be estimated. This means the gradient estimation of the linear pieces depends on the estimated intercept of the first (forward) or the last (backward) piece. Finally, the two trend pieces before and after each TP are used to estimate the direction of trend change and to estimate NDRI that can be used for further evaluation of the TPs in the time series.

3. Simulation experiment

In this section, the performance of STPD on a large set of simulated PS-InSAR time series is demonstrated, and its results are compared with the results of Pettitt, MRSD, and SCPD. A simulation test is performed to compare the performances of Pettitt, MRSD, SCPD, and STPD for TP detection. The time series are simulated using the following equation:

$$y(x_i) = T(x_i) + S(x_i) + \eta(x_i), \qquad 1 \le i \le n \tag{11}$$

where n is the size of the time series, T is a simulated linear trend that has a random TP, S is seasonal noise, and η is white random noise. In this simulation, n is selected to be 60 that is the size of a 5-year-long monthly segment within one of the windows shown in Fig. 2. The trend component is selected as $T(x_i) = 0$ if $1 \le i \le \tau$, and $T(x_i) = -mx_i + mx_\tau$ if $\tau \le i \le 60$, where m is a random number between 5 and 50 mm/year generated by MATLAB *rand*() function and τ is also a random number between 12 and 49 generated by *rand*(). The white random noise is simulated as $\eta = 2\,randn(60, 1)$, where MATLAB *randn*(60, 1) is a random vector of dimension 60 whose entries are drawn from a standard normal distribution with mean zero and standard deviation one. After the least-squares spectral analysis (Ghaderpour, 2021) of a large randomly selected set of real PS-InSAR time series, it was determined that the segments of PS-InSAR time series may contain seasonal components that often can be estimated as

$$S(x_i) = A_0 \sin(\pi x_i + \theta_0) + \sum_{j=1}^{3} A_j \sin(2\pi x_j + \theta_j) \tag{12}$$

where θ_j are the amplitudes and phases, A_0 accounts for inter-annual cycle (every two years), while A_1, A_2, and A_3 account for annual, semi-annual, and higher frequency seasonal cycles, respectively. The amplitudes and frequencies the seasonal components may change over time; however, they usually can be well approximated by Eq. (12) for 5-year-long segments. For each simulated time series, each of the amplitudes and phases in Eq. (12) is selected randomly using *randn*, where amplitude of annual component is also multiplied by 2 due to a higher chance of existence in real PS-InSAR time series. The seasonal oscillations, particularly the annual cycles, exist in the PS-InSAR time series due to cyclic processes over the year, such as rainfalls and temperature variation from summer to winter. Typically, the amplitude of these cycles is between 5 mm and 10 mm. One of the randomly generated time series (SNR = 1.3) is illustrated in Fig. 3. The estimated trend using the proposed method is illustrated in panel (d) that is approximately the same as the simulated trend shown in panel (a).

In the simulated time series using Eq. (11), SNR is calculated as the L2 norm of T divided by the L2 norm of η. The root mean square error (RMSE) is a comparison metric used in this study defined as

$$\text{RMSE} = \sqrt{\frac{1}{N}\sum_{k=1}^{N}(z_k - \hat{z}_k)^2} \tag{13}$$

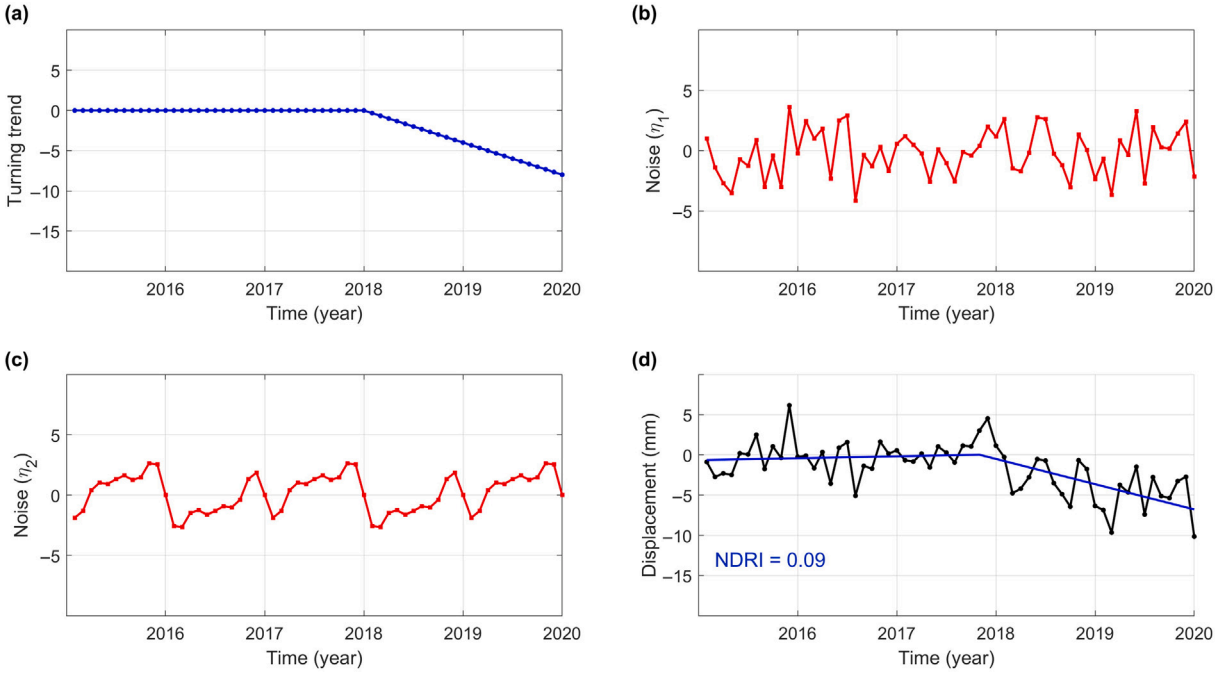

Fig. 3. A simulated example: (a) linear trend with a TP at the beginning of 2018 (T), (b) white random noise (η), (c) seasonal noise (S), (d) sum of the trend and noises (y).

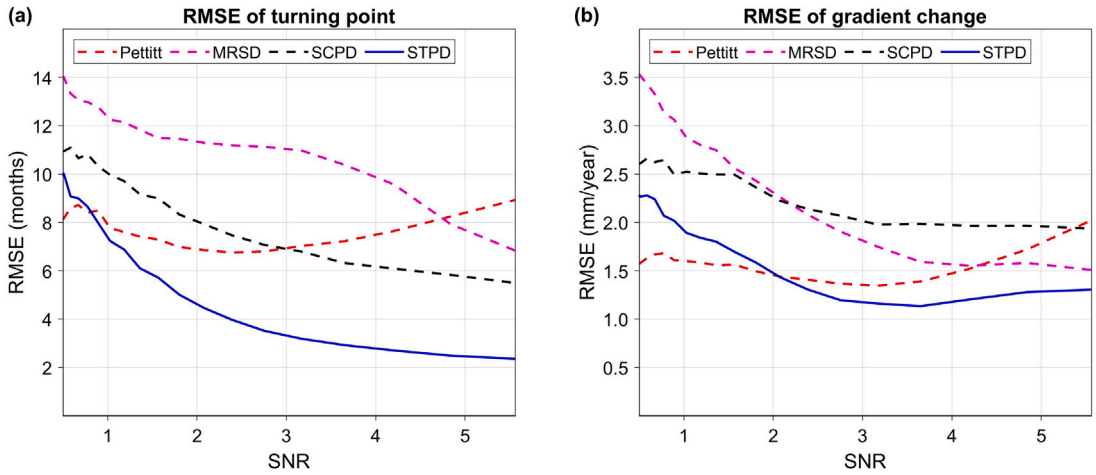

Fig. 4. RMSEs of TP (a) and gradient change or turning direction (b) for Pettitt, MRSD, SCPD, and STPD. The TPs considered in these graphs were statistically significant at 99% confidence level for all the methods.

where N is the number of simulated time series, z_k is the true TP (simulated) and $\hat{z}_k$ is the TP estimated by a method for time series k. To evaluate the performance of estimated gradients, RMSE is also calculated for turning directions corresponding to the estimated TPs. A turning direction is the gradient of the linear piece after the TP minus the gradient of the linear piece before the TP. For the turning direction in these simulations, in Eq. (13), z_k is the simulated direction ($z_k = m_k - 0$), and $\hat{z}_k$ is the estimated direction ($\hat{z}_k = \hat{m}_{k_2} - \hat{m}_{k_1}$). One hundred thousand time series $N = 100,000$ are generated randomly using Eq. (11), and the true SNR vs RMSE graphs for all the four methods are calculated and illustrated in Fig. 4. From this figure, STPD outperformed other methods in terms of RMSE for detecting the true location of the TP and when SNR > 2, STPD also outperformed Sen's slope estimator associated with Pettitt's detected CPs. For a fair comparison, only the TPs were considered that were statistically significant at 99% determined from the statistical tests associated with each method.

To test the sensitivity and specificity of Pettitt and STPD, one hundred thousand time series are randomly simulated using Eq. (11) with $n = 60$ (5-year-long) for two cases: (1) when the time series have a randomly located TP with a turning direction whose absolute value is greater than 1 mm/year, and (2) when the time series have no TPs with gradient varying from zero to 5 mm/year. Table 1 shows the confusion matrices after this process at 99% confidence level for both methods. For a fair and better evaluation when calculating the confusion matrices, a CP or TP was considered truly predicted if its location to the true location of TP was within 6 points or half a year at 99% confidence level for both methods. The overall accuracy, i.e., the average of the diagonal entries in the confusion matrix, for detecting a CP (either jump or TP) by Pettitt is 65% where the differentiation between the two types remains a challenge while the overall accuracy of STPD for detecting solely a TP (no jump) is 83%. It is worth nothing that the false negative rate of Pettitt's test increases as the gradient of randomly simulated time series with no TPs increases.

Table 1
Confusion matrices for Pettitt and STPD for detecting TP in simulated monthly time series of 5-year-long duration. Note that CP means change point which could be a jump or a TP. A CP or TP is truly predicted if its location to the true location of TP is within 6 points or half a year.

Pettitt		Predicted	
		CP	No CP
Actual	Turn	56%	44%
	No Turn	26%	74%

STPD		Predicted	
		Turn	No Turn
Actual	Turn	81%	19%
	No Turn	15%	85%

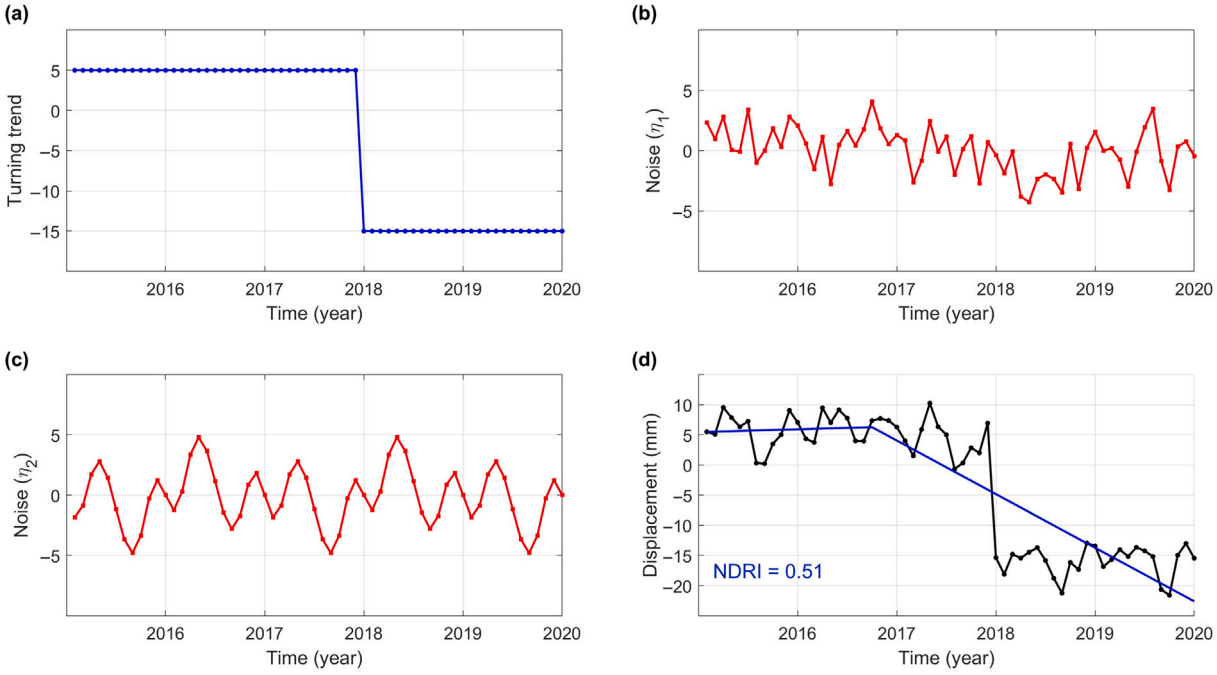

Fig. 5. A simulated example: (a) linear trend with a jump (datum shift) at the beginning of 2018, (b) white random noise (η_1), (c) seasonal noise (η_2), (d) sum of the trend and noises and an estimated trend using STPD with an incorrect TP detected without applying an optimal threshold for NDRI.

From Fig. 4, STPD outperforms SCPD for estimating the TPs and their directions. Recall that both STPD and SCPD use the L2 norm minimization, but the linear pieces in the STPD are always connected while two independent gradients and intercepts are always estimated in SCPD. In other words, SCPD can detect a change as a result of a jump or a TP; however, STPD is only designed for detecting TP with much higher accuracy compared to SCPD. A question may arise on how STPD performs if there is a jump in a time series rather than a TP. To answer this question, a simulated time series with a jump whose magnitude is 20 mm located at the beginning of 2018 is illustrated in Fig. 5. Note that there is no gradient change (zero direction) in this time series, see panel (a). However, STPD detects a TP toward the end of 2016, see panel (d). The NDRI of the estimated trend is 0.51 due to relatively higher L2 norm of the second piece as the result of the high magnitude jump.

To find an optimal threshold to distinguish jumps from TPs when using STPD, one hundred thousand time series are simulated using Eq. (11) with $n = 60$ at random with jumps whose locations and magnitudes are also randomly selected from zero to 50 mm. Then STPD was applied to each simulated time series and its NDRI was estimated to produce the red graph in Fig. 6. Similarly, one hundred thousand simulated time series were simulated using Eq. (11) with $n = 60$ at random but with random TPs and corresponding random directions from zero to 50 mm/year to produce the blue graph in Fig. 6. Note that the seasonal noise and white random noise were also randomly generated for each time series. From Fig. 6, when the absolute value of NDRI is greater than 0.3, a TP was very likely estimated incorrectly due to jump with magnitude greater than 10 mm. Furthermore, all the true TPs have |NDRI| < 0.3, see the blue graph. In PS-InSAR time series, jumps with magnitudes less than 10 mm may appear due to errors during phase unwrapping, or atmospheric noise, etc. Therefore, 0.3 is chosen as an optimal threshold for |NDRI| to separate jumps from TPs.

4. Study region and datasets

The province of Frosinone is in the Lazio region of Italy and has an area of 3247 km^2 and a total population of 493,605 people estimated in 2016 (https://demo.istat.it/). The province is bounded by mountain ranges, the Ernici mountains in the north, the Mainarde in the northeast, the Ausoni and Aurunci mountains in the south, and the Lepini mountains in the southwest, following the natural mountain range development of Italian peninsula, Fig. 7. The main two mountain systems of this province are part of the central Apennines (north) and the Lazio pre-Apennines (south), divided by the low and middle Latin Valley crossed by the Sacco and Liri rivers, Fig. 7c. There are numerous industrial settlements along Sacco river (Massimo et al., 2014). Improper managements and industrial activities for decades affected the Sacco river valley, a vast territory between the provinces

Table 2
Datasets utilized in this study and their brief descriptions. The last access for all datasets was on August 1st, 2023.

Dataset	Spatial Resolution	Dates	Description	Source/Reference
Digital Elevation Model (DEM)	10 m	2023	TINITALY	Tarquini and Nannipieri (2017) and Tarquini et al. (2023)
Land cover/use	100 m	2018	CORINE (Coordination of Information on the Environment) land cover product has 44 land cover classes	https://land.copernicus.eu/pan-european/corine-land-cover
PS-InSAR	20 m in azimuth by 5 m in ground-range	2015–2021 (6-day)	Pre-processed 340 ASC and 208 DESC PS-InSAR time series for periods 04/2015–12/2021 and 01/2015–12/2021, respectively	– European Space Agency (ESA)
Precipitation	4 weather stations	Monthly 01/2015 – 12/2021	Datasets for Cassino, Sora, Frosinone, and San Vito Romano	https://www.3bmeteo.com

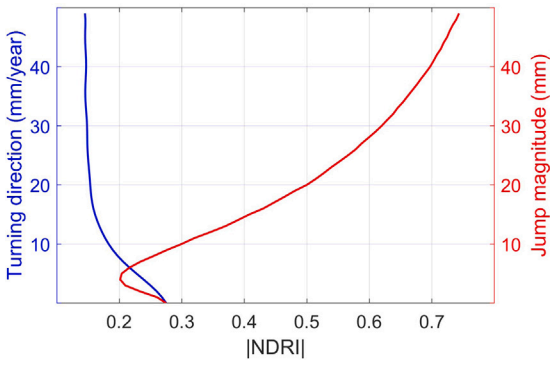

Fig. 6. The absolute value of NDRI vs TP direction in blue and vs jump magnitude in red. When |NDRI| < 0.3, jumps with magnitudes greater than 10 mm can be masked while the TPs remain intact.

of Rome and Frosinone, and produced an unprecedented environmental and social disaster. In addition, this region appeared to be affected by many landslides in forms of slow earth-flow, shallow landslides, and complex movement (Gravina et al., 2017). The datasets employed in this study are listed in Table 2.

5. Field results

In this section, STPD is applied to real PS-InSAR time series for both ascending and descending geometries for the study region, and the estimated TPs are categorized according to topography and land cover/use. Furthermore, correlations between the estimated TPs of PS-InSAR and accumulated precipitation time series are demonstrated within an area susceptible to landslides.

5.1. PS-InSAR trend turning point detection analysis

The STPD was applied to 694,040 ascending and 879,590 descending PS-InSAR time series, and only the time series with at least one statistically significant TP at 99% confidence level with absolute value of direction greater than 1 mm/year are selected such that NDRI < 0.3 and SNR > 1. Totals of 126,777 ascending and 182,621 descending PS-InSAR time series passed these conditions, i.e., about 18% and 20% ascending and descending PS-InSAR time series. The elevation, slope, and land cover/use maps shown in Fig. 7 were utilized to determine the elevation, slope, and land cover/use classes of PS-InSAR locations to produce the bar charts in Fig. 8. From panels (a) and (b) in Fig. 8, about 70% of PS-InSAR time series with the significant TPs have elevation less than 400 m above the mean sea level and slope less than 10 degrees that are mainly in urban and industrial areas.

5.2. PS-InSAR trend turning points within an area of interest (AOI)

To show an application of STPD, an AOI susceptible to landslides is used that has 1345 polygons. These polygons are obtained contouring the areas where PS-InSAR time series have absolute value of velocity greater than 2.5 mm/year, clustered based on a maximum distance of 200 m with minimum of 4 PS. In addition, the polygons are selected such that they do not fall within industrial areas, quarry, mines, or dumps, and the PS locations inside the polygons have minimum slope of 5° (Martino et al., 2022). The information about the number of polygons defined based on ascending and descending PS is given in Table 3.

It was found that 27% of the ascending and 40% of the descending PS-InSAR time series had statistically significant TPs that are potentially due to landslides. The dates of the detected TPs are classified for years 2016, 2017, 2018, 2019, and 2020, excluding 2015 and 2021 due to large uncertainties. The results are shown in Fig. 9 which includes both TPs in ascending and descending geometries.

Two polygons are selected as an example of the TP results. An ascending and a descending PS-InSAR time series with significant TPs are selected for each polygon, and the TP results are illustrated in Fig. 10, marked in Fig. 7b. Generally, the lower the NDRI and the higher the SNR, the more accurate the estimated TPs. Note that there were polygons that contained only ascending PS and polygons that contained only descending PS. Not many areas had both ascending and descending PS less than 50 m apart for a more rigorous slope movement analysis which is a major limitation of PS data.

Time series labeled by A and B located inside an AOI polygon in Fig. 10 have a common detected TP in August 2017 where ASC and DESC time series have positive and negative gradients after the TP, respectively. The time series labeled by C and D located inside another AOI polygon, each has two detected TPs, where the gradient of D is significantly decreasing after September 2017. To justify the simulation criteria described in Section 3, the least-squares spectra (Ghaderpour, 2021) of the monthly resampled PS-InSAR time series after removing the trends are also displayed in Fig. 11, showing statistically significant annual spectral peak for time series B and C at 99% while semi-annual cycle of D is significant at 95%. There were many other PS-InSAR time series with statistically significant inter-annual (0.5 cycles/year) and seasonal cycles (e.g., 1,2,3 cycles/year) as well that were not shown here for brevity.

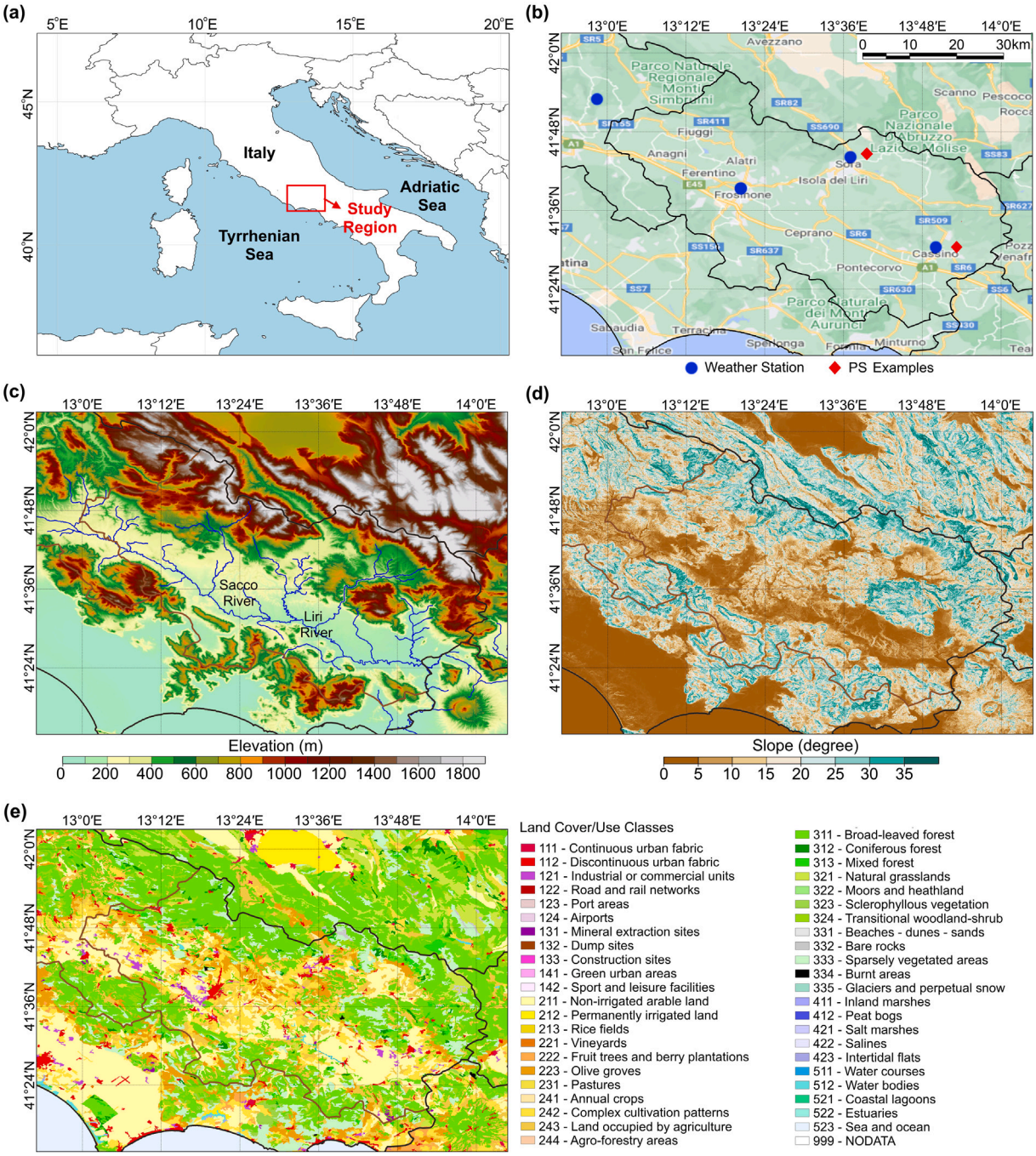

Fig. 7. The study region. (a) A continental map showing the study region inside the red box, (b) Google road map with two PS locations used as examples of PS-InSAR time series, (c) A 10 m resolution DEM of the study region with an overlaid river network, (d) A topographic slope calculated from the DEM map by QGIS, and (e) CORINE land cover/use map at 100 m resolution with 44 classes, updated in 2018.

Table 3
Information about the AOI and PS-InSAR time series for ascending and descending orbits.

Geometry	Number of polygons in AOI	Number of PS	Number of PS with TPs	Number of PS with significant TPs after applying SNR > 1 and NDRI < 0.3
Ascending	641	4656	2911 (64%)	1243 (27%)
Descending	704	4020	3371 (84%)	1597 (40%)

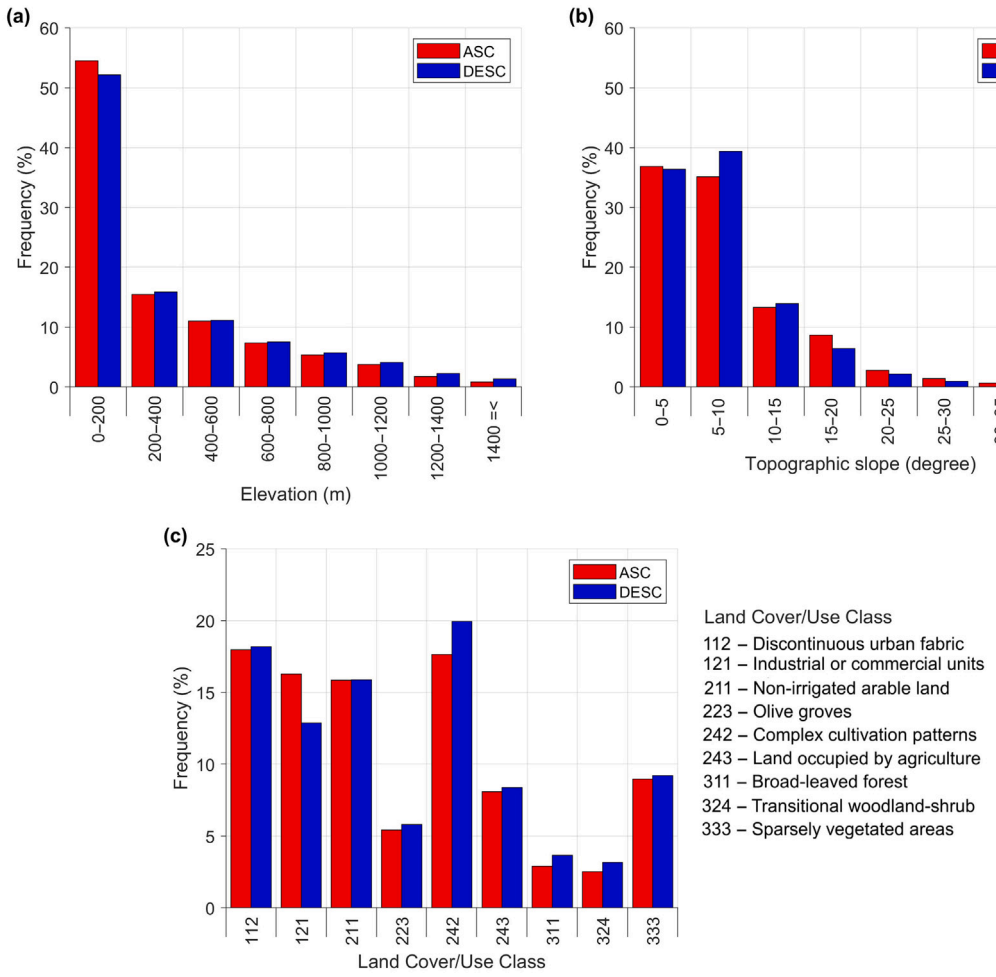

Fig. 8. Bar charts showing the number of PS-InSAR time series (frequency) with significant TPs for each (a) elevation, (b) topographic slope, and (c) land cover/use class shown in Fig. 7. All the PS-InSAR time series within the study region are considered.

6. Discussion

6.1. Theoretical aspects of turning points

The statistical significance of the gradient change in Eq. (8) is based on the normality assumption of the residual series. In practice, however, this assumption may not always hold true due to existence of seasonality and/or serial correlation. Therefore, the test statistics and reported degrees of freedom are considered "naive", providing results that are too liberal; i.e., it can result in more frequent rejection of the null hypothesis H_0 (Santer et al., 2000). The criteria of SNR > 1 and approximately the same forward and backward TP estimation in STPD, can effectively reduce the false positive rate as compared to non-parametric tests, such as Pettitt's test, Table 1. Moreover, Fig. 4 showed that the RMSEs of TPs and their corresponding directions for STPD are significantly lower than the ones for MRSD, SCPD, and Pettitt's method, showing the robustness of STPD. Comparing the estimated TPs using SCPD and MRSD as in Fig. 4a, one can also observe that the mathematical metric (e.g., maximizing gradient difference vs minimizing L2 norm) for estimating CPs can also make a big difference.

On the other hand, presence of gaps or missing values in time series could introduce significant biases on the trend estimation, especially for time series with seasonality. Ahmed et al. (2023) showed that in such time series, ALLSSA can perform significantly better than the least-squares linear regression and Sen's slope estimator for estimating gradients. In JUST, the degrees of freedom reduces as the number of significant constituents increases during the ALLSSA process, providing less liberal and more accurate change detection results. However, the computational cost of ALLSSA can be significantly higher than the simple trend fit model (Ghaderpour and Vujadinovic, 2020). An alternative way for significantly reducing the computational cost and improving the accuracy of CP detection would be regular re-sampling of PS-InSAR data by the spline or other similar interpolation methods which can reduce the effect of outliers and biases in trend estimation when applying fast and simple trend fitting models like STPD.

An effective window size is another important parameter for TP estimation (Ghaderpour and Vujadinovic, 2020; Hussain et al., 2021). For estimating gradual trend change, a 5-year-long window is recommended which is long enough to account for noise including inter-annual, annual, and seasonal noise and short enough to consider multiple TPs between years. This selection along with the translating step of one year allowed rigorous estimation of TPs that were at least three years apart (assumption), though TPs between one and three years apart could also be detected. The STPD code allows users to choose their own window and step sizes according to particular applications. For a smaller window size, more TPs may be estimated but these estimations are more sensitive to noise and seasonality, like other windowing strategies for CP detection (Zuo et al., 2019; Ghaderpour and Vujadinovic, 2020; Hussain et al., 2021).

6.2. Precipitation: A major triggering factor of displacement turning points

The accumulated precipitation time series since January 2015 along with their STPD results are shown in Fig. 12. The window and step sizes

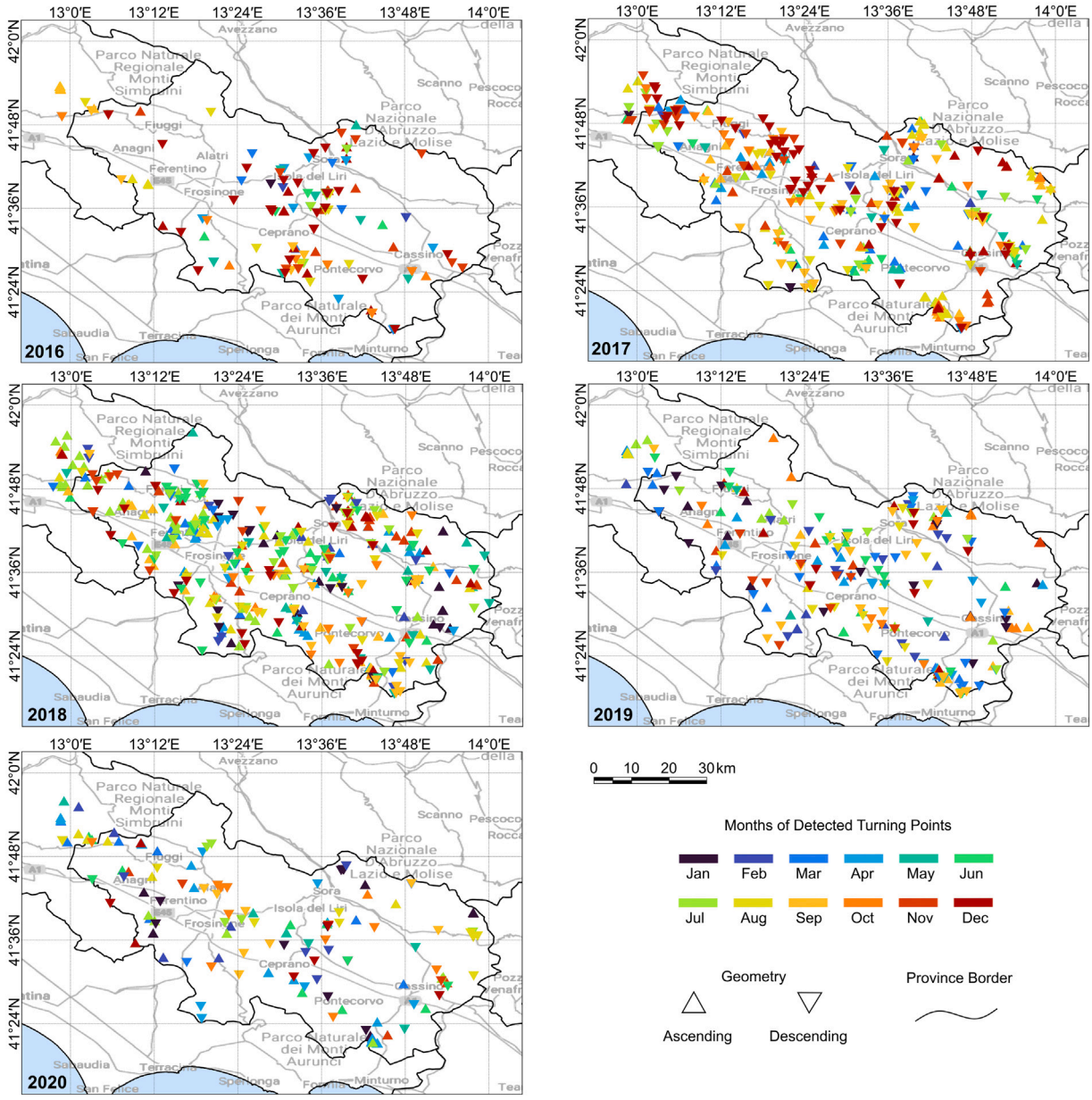

Fig. 9. The dates of the significant TPs for the AOI using STPD for both ascending and descending PS-InSAR time series. Note that the PS locations are within the polygons susceptible to landslides.

for STPD are selected as 3 years and 6 months, respectively, allowing the detection of TPs within a year. From Fig. 12, one can observe that the precipitation velocity (gradient) was increased more than twice after August 2017 (close to or more than 2 m/yr, see the arrows) and again increased since 2020 for all the four locations. This may justify the detected TPs in August and September 2017 for time series shown in Fig. 10 and many other PS shown in Fig. 9.

The frequency bar chart of the TPs for all the PS locations in AOI within 20 km from the weather stations and for the entire AOI are illustrated in Fig. 13. One can see from this figure that many PS-InSAR time series had a TP in August 2017 likely due to increased rainfalls during 2018 and the end of 2017. In fact, all the four locations and in general the province of Frosinone experienced relatively much drier period from Fall 2016 to Fall 2017, immediately followed by a relatively much wetter period from Fall 2017 to 2019, i.e., more than twice precipitation gradient. Tichavský et al. (2019) pointed out that dry spells preceding triggering rainfall may increase slope predisposition to sliding in central Europe which agrees with our results. On the other hand, Ghaderpour et al. (2023) discussed that the gradual warming and dry conditions in most parts of Italy have been and likely to be creating more extreme rainfall events which may increase landslide occurrences, particularly in central Italy.

6.3. Key findings, recommendations, and future direction

The proposed STPD can estimate TPs in a time series faster and more accurately than other change detection methods. The STPD estimates the dates when the gradient of linear trend changes without any jumps or discontinuities. A practical application of STPD is estimating the start times of gradient change in InSAR displacement time series because of slow-moving landslides, ground subsidence or uplift. Lu et al. (2019) proposed an Optimized Hot Spot Analysis (OHSA) on persistent scatterers (PS) and distributed scatterers (DS) datasets to spatially identify hot spots that may represent slow-moving landslide in the Volterra region, Italy. However, their approach did not approximate the dates when landslides started. The hot spot maps illustrated in Figs. 5 and 6

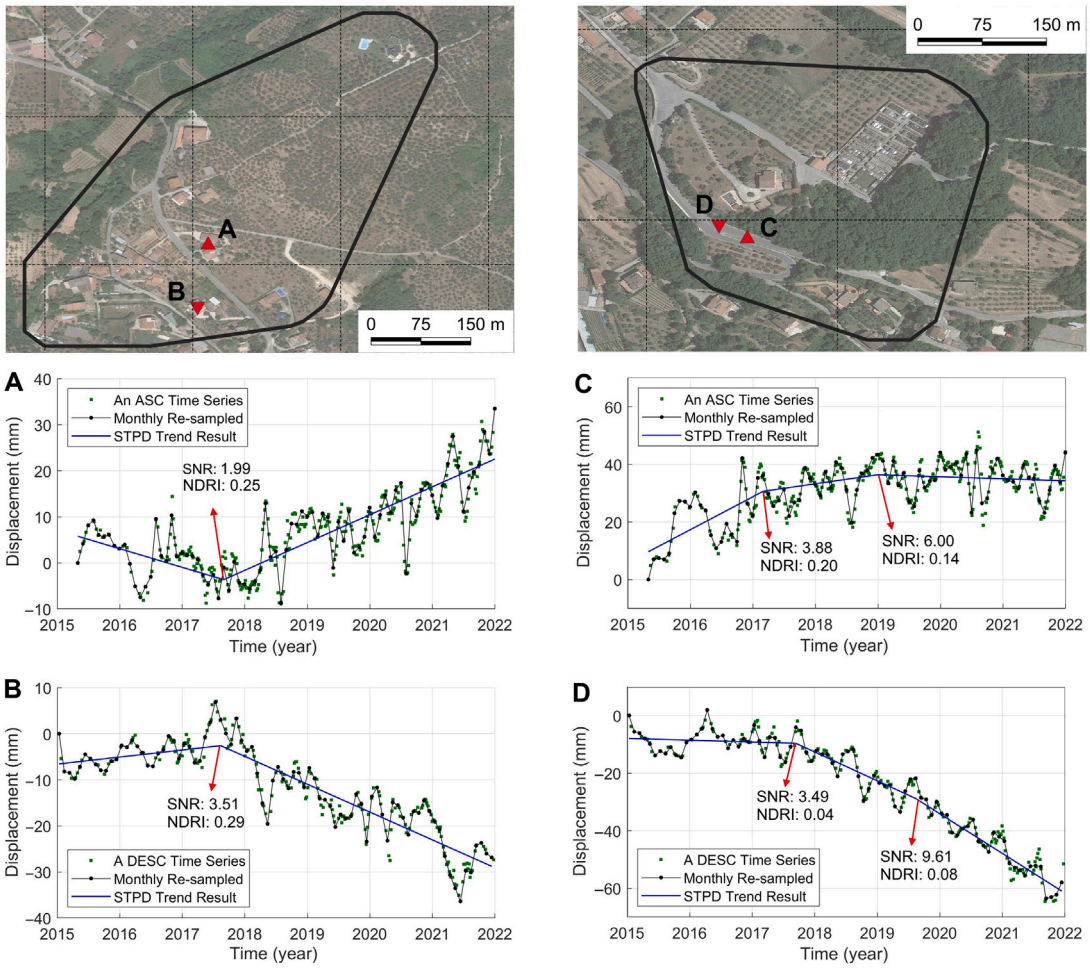

Fig. 10. An example of two polygons susceptible to landslides in the study region, showing PS-InSAR time series with statistically significant TPs.

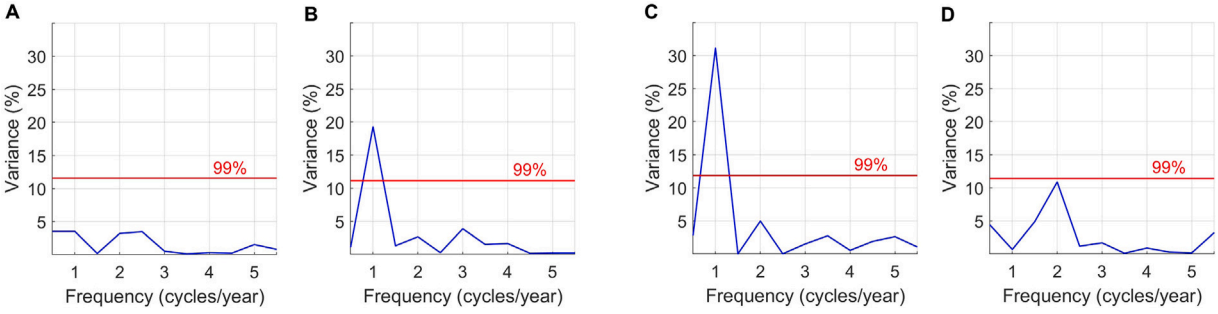

Fig. 11. The residual least-squares spectra of the PS-InSAR time series shown in Fig. 10 (with the same labels A, B, C, D). The red lines represent the critical values at 99% confidence level.

in Lu et al. (2019) only show the hot spot PS/DS, without the dates when slow-moving landslides started. It is worthwhile noting that a displacement time series can have a decreasing trend followed by an increasing trend or vice versa that may result in an overall zero velocity that could be misleading when applying methods such as OHSA. On the other hand, STPD can estimate the potential TPs within each displacement time series and estimate the velocities before and after the TPs. The STPD in conjunction with OHSA could further improve the spatiotemporal accuracy of slow-moving landslide mapping that is subject to future study.

In the present work, STPD was applied to over one million PS-InSAR time series first, then the estimated TPs were classified by topography and land cover/use. As a potential application to landslide monitoring, an AOI susceptible to landslides was determined, and the PS-InSAR time series within that AOI were further analyzed along with potential triggering factors of their trend change (e.g., precipitation). It is worthwhile mentioning that groundwater level variations due to industrial and irrigation activities are also possible reasons for the detected TPs in PS-InSAR time series as illustrated in Fig. 8, mainly in urbanized, industrial, and agricultural areas (Salvati and Zitti, 2009; Piscopo et al., 2022). An accurate spatiotemporal ground deformation mapping is an important task for developing a sustainable environment, urban planning, and mitigating various geohazards, such as groundwater arsenic contamination that is a major global concern (Teixeira et al., 2020; Koley, 2023).

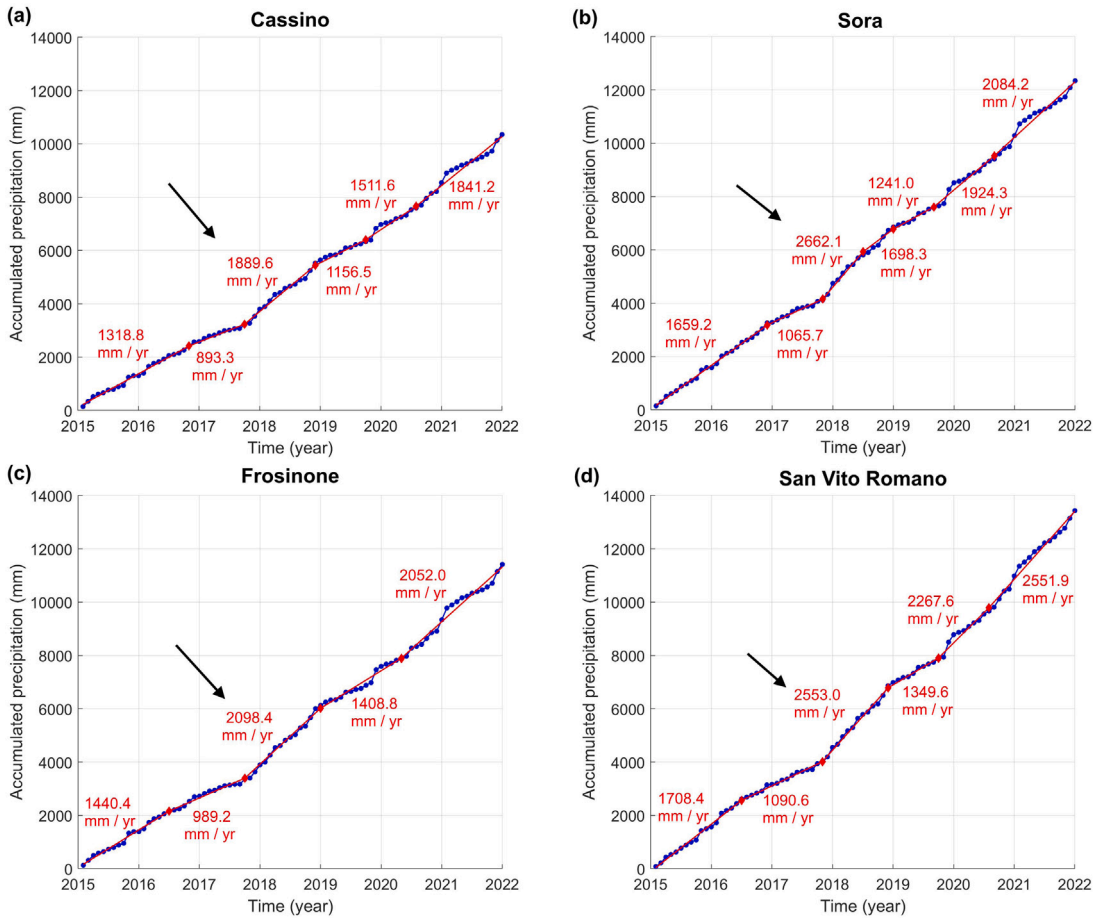

Fig. 12. Accumulated precipitation time series with their estimated TPs by STPD. All the four time series show a significant gradient (velocity) increase from September 2017 to January 2019 (close to or more than 2 m/yr, see arrows).

7. Conclusions

A fast and robust method, namely, sequential turning point detection (STPD), was developed and successfully applied to simulated and real displacement time series. The STPD can process one million PS-InSAR time series of size 100 within one hour in MATLAB and within four hours in Python on an average desktop computer, e.g., Intel (R) Core (TM) i7-7700 CPU @3.6 GHz. Using simulation experiment, it was shown that STPD outperformed other change detection methods in terms of RMSE of the locations and directions of TPs and achieved an overall accuracy of 83%. Furthermore, a statistical metric, namely, NDRI, was introduced to eliminate those TPs that were incorrectly estimated due to presence of jumps or poor data quality.

The detected TPs were also classified according to elevation, slope, and land cover/use. Over 70% of the significant TPs were located on areas with slope less than 10° and elevation less than 400 m, likely as the result of change in groundwater level and anthropogenic activities. Then AOI polygons susceptible to landslides were utilized, and the displacement gradient change of the PS-InSAR time series within these polygons were correlated with accumulated precipitation gradient change. It was found that precipitation was a major triggering factor of slow-moving landslides (shallow landslides, slow earth-flow, etc.). Although monitoring ground deformation through satellite sensors is one effective approach, other methods of monitoring, e.g., ground-based measurements, need to be combined for a more effective and reliable monitoring. It is hoped that the proposed TP detection method and presented results can help geologists, hydrologists, and other scientists and engineers in their research as well as stakeholders and responsible authorities for hazard management and building a sustainable environment.

CRediT authorship contribution statement

Ebrahim Ghaderpour: Writing – original draft, Conceptualization, Methodology, Data curation, Formal analysis, Software. **Benedetta Antonielli:** Writing – review & editing, Conceptualization, Data curation. **Francesca Bozzano:** Writing – review & editing, Conceptualization. **Gabriele ScarasciaMugnozza:** Writing – review & editing, Conceptualization. **Paolo Mazzanti:** Writing – review & editing, Conceptualization.

Declaration of competing interest

The authors declare that they have no known competing financial interests or personal relationships that could have appeared to influence the work reported in this paper.

Data availability

Data will be made available on request.

Acknowledgments

The authors thank Next Generation EU for their financial support.

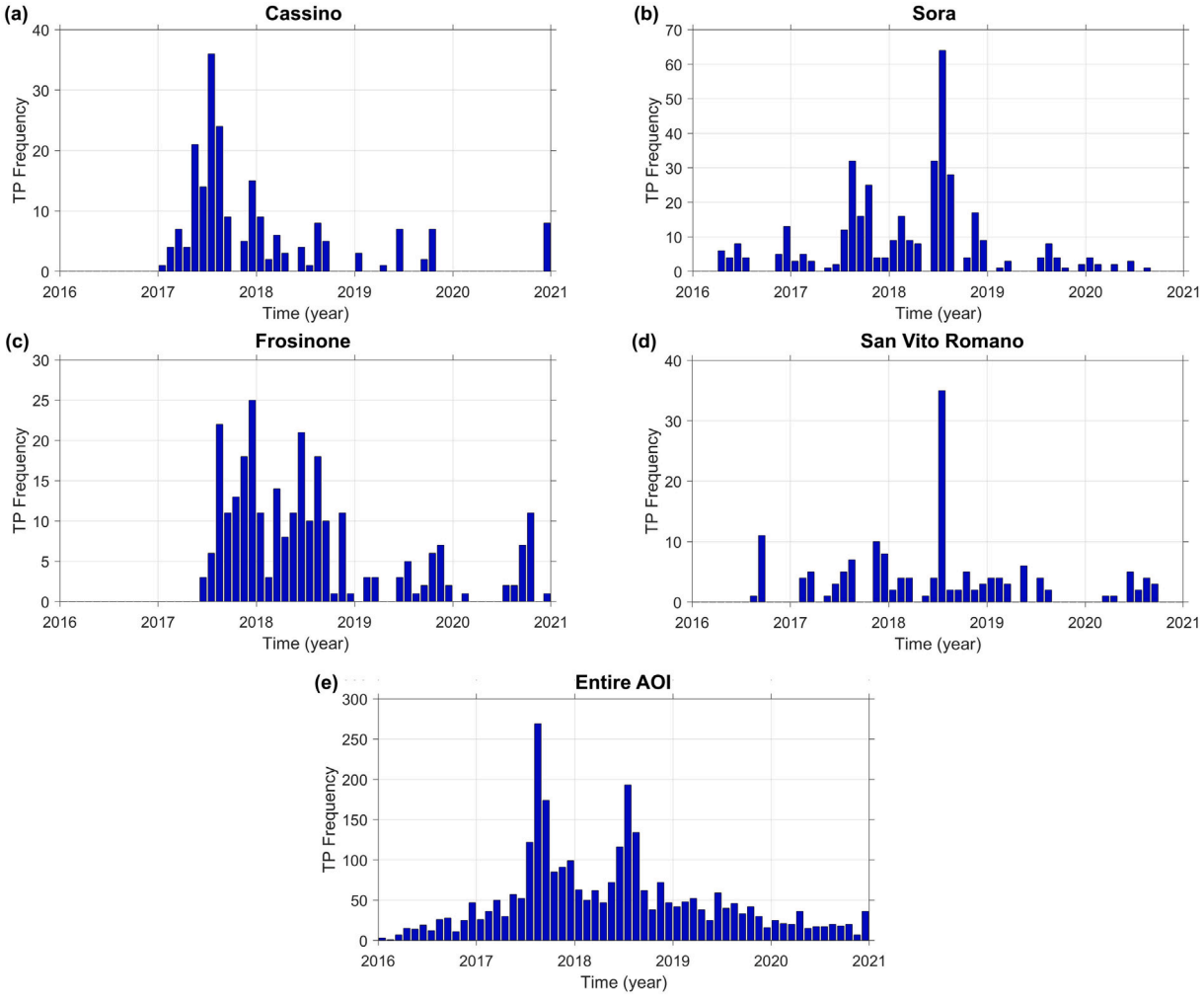

Fig. 13. The frequency of PS-InSAR TPs, shown by different colors in Fig. 9, where the PSs are (a)–(d) within 10 km from the weather stations shown in Fig. 7b, and (e) for the entire AOI.

Funding

This study was carried out within the Spoke VS2 Ground Instabilities of the RETURN Extended Partnership and received funding from the European Union Next-Generation EU (National Recovery and Resilience Plan – NRRP, Mission 4, Component 2, Investment 1.3 – D.D. 1243 2/8/2022, PE0000005).

Code availability

Name of the code/library: STPD
Contact: ebrahim.ghaderpour@uniroma.it
Hardware requirements: Laptop or PC with Windows or Linux
Program language: MATLAB and Python
Software required: Basic and commonly used libraries in MATLAB and Python
Program size: 2.5 megabytes
The source code is available at: https://github.com/Ghaderpour/LSWAVE-SignalProcessing

References

Ahmed, M.R., Ghaderpour, E., Gupta, A., Dewan, A., Hassan, Q.K., 2023. Opportunities and challenges of Spaceborne sensors in delineating land surface temperature trends: A review. IEEE Sens. J. 23, 6460–6472.

Allocca, V., Coda, S., Calcaterra, D., De Vita, P., 2022. Groundwater rebound and flooding in the Naples' periurban area (Italy). J. Flood Risk Manag. 15, e12775.

Aminikhanghahi, S., Cook, D.J., 2017. A survey of methods for time series change point detection. Knowl. Inf. Syst. 51, 339–367.

Awty-Carroll, K., Bunting, P., Hardy, A., Bell, G., 2019. An evaluation and comparison of four dense time series change detection methods using simulated data. Remote Sens. 11, 2779.

Bai, L., Jiang, L., Wang, H., Sun, Q., 2016. Spatiotemporal characterization of land subsidence and uplift (2009–2010) over Wuhan in Central China revealed by TerraSAR-X InSAR analysis. Remote Sens. 8, 350.

Cascini, L., Fornaro, G., Peduto, D., 2009. Analysis at medium scale of low-resolution DInSAR data in slow-moving landslide-affected areas. ISPRS J. Photogramm. Remote Sens. 64, 598–611.

Cianflone, G., Conforti, M., Soleri, S., Ietti, F., 2021. Preliminary data on slow-moving landslides-affected urban areas through geological, geomorphological and InSAR analysis. Ital. J. Eng. Geol. Environ. 12, 21–33.

Cianflone, G., Tolomei, C., Brunori, C.A., Dominici, R., 2015. InSAR time series analysis of natural and Anthropogenic Coastal plain subsidence: The case of Sibari (Southern Italy). Remote Sens. 7, 16004–16023.

Coda, S., Confuorto, P., De Vita, P., Di Martire, D., Allocca, V., 2019. Uplift evidences related to the recession of groundwater abstraction in a Pyroclastic-Alluvial Aquifer of Southern Italy. Geosciences 9, 215.

De Martino, P., Dolce, M., Brandi, G., Scarpato, G., Tammaro, U., 2021. The ground deformation history of the Neapolitan volcanic area (Campi Flegrei Caldera, Somma–Vesuvius Volcano, and Ischia Island) from 20 years of continuous GPS observations (2000–2019). Remote Sens. 13, 2725.

Ghaderpour, E., 2021. JUST: MATLAB and Python software for change detection and time series analysis. GPS Solut. 25, 85.

Ghaderpour, E., Mazzanti, P., Scarascia Mugnozza, G., Bozzano, F., 2023. Coherency and phase delay analyses between land cover and climate across Italy via the least-squares wavelet software. Int. J. Appl. Earth Obs. Geoinf. 118, 103241.

Ghaderpour, E., Pagiatakis, S.D., Hassan, Q.K., 2021. A survey on change detection and time series analysis with applications. Appl. Sci. 11, 6141.

Ghaderpour, E., Vujadinovic, T., 2020. Change detection within remotely-sensed satellite image time series via spectral analysis. Remote Sens. 12, 4001.
Gourgouletis, N., Baltas, E., 2023. Investigating hydroclimatic variables trends on the natural lakes of western Greece using earth observation data. Sensors 23, 2056.
Gravina, T., Figliozzi, E., Mari, N., Schinosa, F.D.L.T., 2017. Landslide risk perception in Frosinone (Lazio, Central Italy). Landslides 14, 1419–1429.
Hussain, M.A., Chen, Z., Zheng, Y., Shoaib, M., Ma, J., Ahmad, I., Asghar, A., Khan, J., 2022. PS-InSAR based monitoring of land subsidence by groundwater extraction for Lahore Metropolitan City, Pakistan. Remote Sens. 14, 3950.
Hussain, E., Novellino, A., Jordan, C., Bateson, L., 2021. Offline-online change detection for Sentinel-1 InSAR time series. Remote Sens. 13, 1656.
Jaiswal, R.K., Lohani, A.K., Tiwari, H.L., 2015. Statistical analysis for change detection and trend assessment in climatological parameters. Environ. Process. 2, 729–749.
Koley, S., 2023. Arsenic calamity in India's West Bengal: A critical review of mitigation scenarios. Proc. Inst. Civ. Eng. - Eng. Sustain. 176 (4), 198–213.
Kundu, J., Sarkar, K., Ghaderpour, E., Scarascia Mugnozza, G., Mazzanti, P., 2023. A GIS-based kinematic analysis for jointed rock slope stability: An application to Himalayan slopes. Land 12, 402.
Lattari, F., Rucci, A., Matteucci, M., 2022. A deep learning approach for change points detection in InSAR time series. IEEE Trans. Geosci. Remote Sens. 60, 5223916.
Li, S., Pi, H., 2022. Deconstruction of dryness and wetness patterns with drought condition assessment over the Mun River Basin, Thailand. Land 11, 2244.
Lu, P., Bai, S., Tofani, V., Casagli, N., 2019. Landslides detection through optimized hot spot analysis on persistent scatterers and distributed scatterers. ISPRS J. Photogramm. Remote Sens. 156, 147–159.
Makabayi, B., Musinguzi, M., Otukei, J., 2021. Estimation of ground vertical displacement in Landslide Prone Areas using PS-InSAR. A Case Study of Bududa, Uganda. Int. J. Geosci. 12, 347–380.
Mann, H.B., Whitney, D.R., 1947. On a test of whether one of two random variables is stochastically larger than the other. Ann. Math. Stat. 18, 50–60.
Martino, S., Fiorucci, M., Marmoni, G.M., Casaburi, L., Antonielli, B., Mazzanti, P., 2022. Increase in landslide activity after a low-magnitude earthquake as inferred from DInSAR interferometry. Sci. Rep. 12, 2686.
Massimo, A., Dell'Isola, M., Frattolillo, A., Ficco, G., 2014. Development of a Geographical Information System (GIS) for the integration of solar energy in the energy planning of a wide area. Sustainability 6, 5730–5744.
Mateos, R.M., Ezquerro, P., Luque-Espinar, J.A., Béjar-Pizarro, M., Notti, D., Azañón, J.M., Montserrat, O., Herrera, G., Fernández-Chacón, F., Peinado, T., 2017. Multiband PSInSAR and long-period monitoring of land subsidence in a strategic detrital aquifer (Vega de Granada, SE Spain): An approach to support management decisions. J. Hydrol. 553, 71–87.
Moretto, S., Bozzano, F., Mazzanti, P., 2021. The role of satellite InSAR for landslide forecasting: Limitations and openings. Remote Sens. 13, 3735.
Nakileza, B.R., Nedala, S., 2020. Topographic influence on landslides characteristics and implication for risk management in upper Manafwa catchment, Mt Elgon Uganda. Geoenviron. Disasters 7, 27.
Pettitt, A.N., 1979. A non-parametric approach to the change-point problem. J. R. Stat. Soc. Ser. C Appl. Stat. 28, 126–135.
Piscopo, V., Sbarbati, C., Lotti, F., Lana, L., Petitta, M., 2022. Sustainability indicators of groundwater withdrawal in a heavily stressed system: The case of the Acque Albule Basin (Rome, Italy). Sustainability 14, 15248.
Ren, T., Gong, W., Gao, L., Zhao, F., Cheng, Z., 2022. An interpretation approach of ascending–descending SAR data for landslide identification. Remote Sens. 14, 1299.
Salvati, L., Zitti, M., 2009. The environmental "risky" region: Identifying land degradation processes through integration of socio-economic and ecological indicators in a multivariate regionalization model. Environ. Manage. 44, 888–898.
Santer, B.D., Wigley, T.M.L., Boyle, J.S., Gaffen, D.J., Hnilo, J.J., Nychka, D., Parker, D.E., Taylor, K.E., 2000. Statistical significance of trends and trend differences in layer-average atmospheric temperature time series. J. Geophys. Res. 105, 7337–7356.
Shawky, M., Ahmed, M.R., Ghaderpour, E., Gupta, A., Achari, G., Dewan, A., Hassan, Q.K., 2023. Remote sensing-derived land surface temperature trends over South Asia. Ecol. Inform. 74, 101969.
Tarquini, S., Isola, I., Favalli, M., Battistini, A., Dotta, G., 2023. TINITALY, a digital elevation model of Italy with a 10 meters cell size (version 1.1). Istituto Nazionale di Geofisica e Vulcanologia (INGV). http://dx.doi.org/10.13127/tinitaly/1.1.
Tarquini, S., Nannipieri, L., 2017. The 10 m-resolution TINITALY DEM as a transdisciplinary basis for the analysis of the Italian territory: Current trends and new perspectives. Geomorphology 281, 108–115.
Teixeira, M.C., Santos, A.C., Fernandes, C.S., Ng, J.C., 2020. Arsenic contamination assessment in Brazil – Past, present and future concerns: A historical and critical review. Sci. Total Environ. 730, 138217.
Tichavský, R., Ballesteros-Cánovas, J.A., Šilhán, K., Tolasz, R., Stoffel, M., 2019. Dry spells and extreme precipitation are the main trigger of landslides in Central Europe. Sci. Rep. 9, 14560.
Varnes, D.J., 1978. Slope movement types and processes. In: Schuster, R.L. and Krizek, R.J., Eds., landslides, analysis and control, transportation research board, Special Report No. 176. Natl. Acad. Sci. 147, 11–33.
Wang, Z., Lawrence, J., Ghail, R., Mason, P., Carpenter, A., Agar, S., Morgan, T., 2022. Characterizing micro-displacements on active faults in the Gobi Desert with time-series InSAR. Appl. Sci. 12, 4222.
Yao, J., Yao, X., Liu, X., 2022. Landslide detection and mapping based on SBAS-InSAR and PS-InSAR: A case study in Gongjue County, Tibet, China. Remote Sens. 14, 4728.
Zaghloul, M.S., Ghaderpour, E., Dastour, H., Farjad, B., Gupta, A., Eum, H., Achari, G., Hassan, Q.K., 2022. Long term trend analysis of river flow and climate in Northern Canada. Hydrology 9, 197.
Zeyada, H.H., Mostafa, M.S., Ezz, M.M., Nasr, A.H., Harb, H.M., 2022. Resolving phase unwrapping in interferometric synthetic aperture radar using deep recurrent residual U-Net. Egypt. J. Remote. Sens. Space Sci. 25, 1–10.
Zhang, L., Ding, X., Lu, Z., 2011. Modeling PSInSAR time series without phase unwrapping. IEEE Trans. Geosci. Remote Sens. 49, 547–556.
Zuo, B., Li, J., Sun, C., Zhou, X., 2019. A new statistical method for detecting trend turning. Theor. Appl. Climatol. 138, 201–213.